RESEARCH ARTICLE

NANO · MICRO small
www.small-journal.com

Surface Stabilization to Enhance Single Molecule Toroidal Behavior in $\{Dy_3\}$ Molecules: the Impact of Au(111), MgO, and Graphene Surfaces

*Deepanshu Chauhan, Rupesh Kumar Tiwari, and Gopalan Rajaraman**

Single-molecule toroids (SMTs), with vortex-like magnetic anisotropy axes, hold promise for quantum technologies, but controlling their toroidal states on the surface remains challenging. To address this, the SMT behavior of $[Dy_3(\mu_3\text{-}OH)_2L_3Cl(H_2O)_5]Cl_3$ (where L = *ortho*-vanillin) grafted onto Au(111), MgO has been studied, and graphene surfaces in pristine form (1) and with pyrene (2) and $(CH_2)_8S$ (3) linkers, using periodic density functional theory and *ab initio* CASSCF/RASSI-SO methods. Both pristine and chemically functionalized molecules are stable on Au(111) and graphene surfaces; however, functionalization provides higher binding energies and, in some cases, enhances the SMT properties. The MgO surface, however, is found to be unsuitable as it abstracts an H atom from the molecule, leading to the loss of its SMT characteristics. The energy gap (ΔE) between the toroidal (nonmagnetic) and spin-flip (magnetic) states in complex 1 on Au(111) and graphene surfaces are 6.9 and 6.6 cm^{-1}, respectively. Complexes 2 on Au(111) and 3 on graphene exhibit ΔE and toroidal blocking fields of 9.8 cm^{-1}/1.2 T and 6.8 cm^{-1}/0.83 T, respectively, representing the highest recorded values for this class of SMTs. These findings demonstrate the potential of surface stabilization to improve the functionality and applicability of SMTs in advanced quantum technologies.

1. Introduction

Molecules possessing a permanent dipole moment generate an electric field.[1] Following the basic right-hand thumb rule, the propagation of the electric field leads to creating an inherent magnetic field perpendicular to the electric field's direction.[2] Similarly, molecules possessing permanent magnetic moment, if arranged in a vortex manner, generate toroidal moment perpendicular to the plane of the magnetic field and have garnered a large interest since its experimental observations in $LiCoPO_4$.[3,4] This toroidal moment was well known in classical physics as a name of anapole moments.[5,6] Although many 3D solid-state materials have been found to exhibit toroidal moments,[7] their discovery has often been incidental, as a systematic methodology for inducing such phenomena in these materials is still lacking, and microscopic theoretical understanding is the need of the hour, as highlighted by Spaldin and co-workers.[8] Additionally, Wang et al. have explored the dynamical control of toroidal moments in Tb(III) based molecular systems.[9] Still, a clear, deliberate approach to induce toroidal moments in solid-state structures remains elusive.[9] The very first example of the observation of toroidal moment in a molecular system was reported in $[Dy_3(\mu_3\text{-}OH)_2L_3Cl(H_2O)_5]Cl_3\cdot 4H_2O\cdot 2MeOH\cdot 0.7MeCN$ (L = *ortho*-vanillin) (referred as **1** throughout the manuscript) where both experiment and theoretical calculations proposed the existence of toroidal states.[10–14] Subsequently, several molecular Dy(III) complexes were reported to exhibit toroidal moments, commonly called single-molecule toroids (SMTs).[15] Since toroidal moments result in bistable pro- and con-rotating states, they are also called spin chirality.[14] Despite thousands of Ln(III) complexes, the number of molecules possessing SMT behavior is still limited, and the criteria to observe toroidal moments are rather stringent.[16] As molecules often are asymmetric and there is no easy recipe to place the Ln(III) Ising magnetic anisotropy (g_z) axis along the vortex plane for all the ions; important criterion to achieve net zero toroidal states.[16] It is well established in the Dy(III) single molecule magnet (SMM) area that the Ising type anisotropy is extremely sensitive to the ligand environment,[17–20] and this is especially true also for SMTs with the additional complexity of inter/intramolecular interactions and temperature playing a role in their observations.[21,22] To date, there are various metal cores have been synthesized to stabilize the toroidal ground state,[15,23] starting from $\{Dy_3\}$,[16,24,25] $\{Dy_4\}$,[26,27] $\{Dy_6\}$,[28–30] $\{Dy_8\}$,[31] $\{Dy_3+Dy_3\}$,[32,33] {3d-4f}[34–37] and especially the coupling of both the triangles through a 2p/3d metal ions $\{MLn_6\}$, which found to exhibit Ferrotoroidal ground state.[38,39] Further, there is also a report of $\{Dy_4\}$ cubane exhibiting 3D toroidal moment, which does not necessitate having all the Ln(III) ions in the same molecular plane.[40] Toroidal moments emerge from the intricate interplay between electric

D. Chauhan, R. K. Tiwari, G. Rajaraman
Department of Chemistry
Indian Institute of Technology Bombay Powai
Mumbai, Maharashtra 400076, India
E-mail: rajaraman@chem.iitb.ac.in

The ORCID identification number(s) for the author(s) of this article can be found under https://doi.org/10.1002/smll.202412283

DOI: 10.1002/smll.202412283

and magnetic dipoles, leading to magnetoelectric effects that position them as promising candidates for next-generation data storage devices.[7] Further, SMTs can also be used for quantum spin sensors,[41] transducers, and spin-filtering devices.[42–46] One of the big advantages of employing toroidal moments is the electrical readout of the stored data, which offers a spatiotemporal advantage over conventional magnetic-based storage.[7] However, to realize any potential application for toroidal molecules, it is important to fabricate them on surfaces.[47–49] Among many surfaces that have been successfully tested, the following stand out: (i) Mannini and co-workers demonstrated that $\{Fe_4\}$ SMM maintains their properties when fabricated on an Au(111).[50,51] This preservation of properties is achieved through functionalization using a thioacetyl-terminated alkyl chain, forming a robust chemical bond between sulfur atoms and gold through chemisorption.[50] (ii) Ruben and co-workers illustrated that the $TbPc_2$ molecule retains its characteristics on graphene by functionalizing the phthalocyanine ligand with pyrene rings before being assembled on the graphene surface.[52] Moreover, it has been observed that the magnetic properties of the $TbPc_2$ molecule persist when adsorbed on 2-monolayer MgO(001) film grown over an Ag(001) surface, where MgO serves as a decoupling layer.[53] (iii) Popov and co-workers successfully stabilized a Tb(III) dimer within an endohedral metallofullerene (EMF) on a graphene surface by functionalizing the EMF with a pyrene ring. This system exhibited magnetic bi-stability up to a temperature of 28 K.[54] Several signs of progress have also been made in revealing how grafting SMMs onto surfaces affects their magnetic exchange, as well as their electronic and magnetic properties.[48] Despite several experimental and theoretical studies on toroidal complexes, there are no studies on toroidal molecules on surfaces. This is understandable, considering that less than 1% of polynuclear Ln(III) complexes exhibit toroidal properties.[16] Moreover, these properties are highly sensitive, and even minor structural distortions or modifications often necessary for surface placement can be detrimental to their SMT behavior. This is especially important given that the number of SMMs that failed to exhibit SMM characteristics on surfaces is much larger than those that successfully did, making it a more prominent challenge than SMTs.

Keeping all this in mind, here we have explored the toroidal behavior of $\{Dy_3\}$ complex on various surfaces using a combination of periodic density functional theory (DFT) and ab initio CASSCF/RASSI-SO/POLY_ANISO (CASSCF; complete active space self-consistent field, RASSI-SO; restricted active space state interaction with spin-orbit) calculations to figure out the best combination to retain or even enhance the toroidal properties on the surface. We aim to particularly answer the following intriguing questions: (i) Can the single-ion magnetic behavior be preserved when molecules are anchored onto surfaces? (ii) Is the unique SMT behavior maintained on surfaces such as Au(111), graphene, and MgO? (iii) Does surface alter the intramolecular Dy(III) magnetic coupling?

2. Computational Details

To investigate the SMT behavior of these complexes on surfaces, we targeted **1** in its pristine form, as well as with pyrene (**2**) and $(CH_2)_8S$ (**3**) linkers grafted onto Au(111), MgO and graphene surfaces. Detailed *ab initio* CASSCF calculations and periodic DFT calculations were performed for this analysis. Perdew–Burke–Ernzerhof (PBE) functional and double-ζ-valence-polarized (DZVP) basis sets were used for geometry optimizations and have been chosen based on literature precedent.[55] To account for the core electrons, Geodecker-Tetter-Hutter (GTH) pseudopotentials were used as implemented in the CP2K-6.1.0 suite of programs.[56] A mesh cut-off of 400 eV and force cut-off of 10^{-4} eV $Å^{-1}$ were used throughout. For the Au(111) surface, a supercell of 15 × 14 × 1 dimension (a = b = 2.877 Å) was used, with a vacuum of 15 Å along the Z-direction. Due to the face-centered cubic (*fcc*) structure of Au(111), three atomic layers were suggested earlier.[55] The interatomic distance within each Au layer was 2.349 Å, consistent with previous reports.[57,58] The Au surface was pre-optimized, and during molecule-on-surface optimization, all three layers were frozen. For the graphene surface, a supercell of 16 × 19 × 1 dimension (a = b = 2.467 Å) with a 15 Å vacuum along the Z-direction was used, and full structural relaxation was performed. For the MgO surface, a supercell of 9 × 9 × 1 dimension (a = b = 4.194 Å) with a vacuum of 15 Å along the Z-direction was constructed. The MgO surface adopts a simple cubic structure with an ABAB stacking pattern and was modelled with two layers, as suggested.[59,60] Both MgO layers were fixed during molecule-on-surface optimization. To calculate the magnetic exchange (J) between the metal centers, we have used broken symmetry density functional theory calculations (BS-DFT)[61] employing the widely accepted B3LYP functional and the double-ζ quality basis set employing Cundari–Stevens (CS) relativistic effective core potential on Gd(III),[62] the triple-ζ-valence (TZV) basis set for rest of the atom in the Gaussian 16 suite of programs.[63] This combination of tools has been identified in prior studies as providing the most accurate J values.[64] The binding energies (BEs) of the model complexes **1**, **2**, and **3** on various surfaces were computed using the following equation (1):

$$E_b = E_{AB} - \left(E_A + E_B\right) \quad (1)$$

where E_b corresponds to the BE of the system, E_{AB} is the total energy of the system, E_A is the energy of the surface, and E_B is the energy of the pristine model complex.

To compute the magnetic anisotropy along with the toroidal moment, CASSCF/RASSI-SO/SINGLE_ANISO/POLY_ANISO tools were used as implemented in the MOLCAS 8.2 program.[65] All wave function-based calculations were performed using the state-averaged CASSCF approach with the RASSI-SO.[66,67] For the Dy(III) ion, an active space CAS(9, 7) was used. Douglas–Kroll Hamiltonian (DKH) was used to account for the scalar relativistic effect.[68] Here, we have employed the [ANO-RCC...8s7p5d3f2g1h.] for Dy(III) atoms, the [ANO-RCC...7s6p4d2f.] basis set for La(III) atoms, the [ANO-RCC...4s3p1d.] basis set for Cl atoms, the [ANO-RCC...3s2p.] basis set for O atoms, the [ANO-RCC...3s2p.] basis set for N atom, the [ANO-RCC...3s2p.] basis set for the C atom, and the [H.ANO-RCC...2s.] basis set for H atoms.[69] The resulting spin-orbit (SO) wave functions and energies were employed to compute magnetic anisotropy (g-tensors) for both ground and excited state multiplets using the SINGLE_ANISO module.[70] Dipole-dipole magnetic couplings between the Dy(III) centers

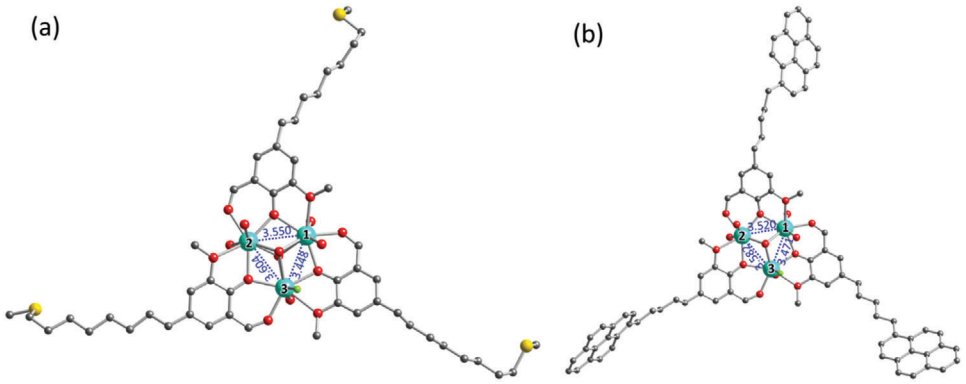

Figure 1. DFT-optimised molecular structures of complexes a) for **2**, and b) for **3** are shown, with the bond lengths between the Dy(III) centers. Color code: Dy(III) (cyan), O (red), C (gray), Cl (green), and S (yellow). Hydrogen atoms are omitted for clarity to focus on the key structural elements.

and magnetic properties of the complexes, encompassing all three Dy(III) centers, were derived using the Lines model within the POLY_ANISO program.[71] (other details in the computational section in ESI). The exchange Hamiltonian employed is shown in the following equation (2):

$$\hat{H} = -J \cdot S_i \cdot S_j \quad (2)$$

here $J = J_{exc.} + J_{dip.,}$ i.e., J is the total magnetic interaction consisting of dipolar ($J_{dip.}$) and the exchange interactions ($J_{exc.}$). The S_i and S_j are the corresponding spin operators. This comprehensive approach facilitated a thorough exploration of the magnetic behavior and properties of the $\{Dy_3\}$ systems, shedding light on its SMT characteristics. For the ab initio calculations, we have mimicked the surface using DFT computed point charges, and this has been shown to yield numerically good results with respect to anisotropy, as demonstrated elsewhere.[72]

3. Results and Discussion

3.1. DFT Analysis of Electronic Structure, Stability, and Binding Energies

Complex **1** has three six-coordinate Dy(III) metal ions, two of them possessing $\{DyO_6\}$ core while the third possessing $\{DyO_5Cl\}$ core, creating asymmetry induced by the ligand environment. To start with, we have performed DFT optimization of complex **1**, and the optimized geometry (**1**^{opt}) was found to have a close resemblance to the X-ray geometry, instilling confidence in the reliability of the chosen methodology (Table S1, Supporting Information). The pristine molecule **1** was also placed on surfaces Au(111), graphene, and MgO to assess and analyze the role of linkers.

In the next step, we anchor these molecules onto surfaces in their pristine form and through functionalization of the *ortho*-vanillin ligand. For this purpose, two modifications were carried out to the ligand: (i) attachment of $(CH_2)_8$−SMe (**2**) to enable anchoring on an Au(111) surface and MgO surface, (ii) attachment of $(CH_2)_5$−pyrene (**3**) group to graft on graphene and MgO surfaces. The choice of the $(CH_2)_8$-S-Me chain length is specifically aligned with the diagonal distance of the molecule (≈11 Å; Figure S1, Supporting Information). A longer chain length also offers: (i) sufficient flexibility without compromising structural integrity, (ii) prevention of bending or distortion upon adsorption on the surface, (iii) mitigation of direct interactions between the OH_2 groups of the molecule and the thiolate sulfur atoms, and (iv) minimization of undesired strong inter-$\{Dy_3\}$...$\{Dy_3\}$ interactions and (v) potential to enhance the magnetic properties. Similarly, we have chosen the $(CH_2)_5$−pyrene as the anchoring group, considering it a π-electronic cloud for strong interaction with graphene and MgO surface (Figure S2, Supporting Information).[53] The DFT-optimized geometries with the anchoring groups are shown in **Figure 1**, and geometrical parameters of **2** and **3** closely resemble that of **1**^{opt}, suggesting that the functionalization of the molecule has not influenced the core geometry significantly (Table S1, Supporting Information).

For an in-depth exploration of the toroidal characteristics on surfaces, **2** was fabricated on Au(111), while **3** was grafted onto Graphene and MgO surfaces. For **2**, two possible geometries were considered: (i) where the Dy(3)–Cl bond is allowed to anchor on the Au(111) surface (referred to as **2′@Au(111)**) and (ii) Dy(3)–Cl is away from the surface (referred as **2@Au(111)** see **Figure** 2a,b). The BE suggests the **2@Au(111)** geometry is favorable by −456.3 kJ mol^{-1} (−877.3 vs −1333.6 kJ mol^{-1}) compared to the former, suggesting stronger anchoring of the molecule when the Dy(3)-Cl is away from the surface. Similarly, we have also attempted the same orientation/geometries on the graphene surface (**3′@graphene** vs **3@graphene**). Here, as well, the **3@graphene** was found to have greater BE by −444.1 kJ mol^{-1} (−637.2 vs −1081.3 kJ mol^{-1}) compared to the **3′@graphene** isomer, consistent with the energies obtained from the Au(111) surface (**3′** see Figure 2c,d). A smaller BE for the **2′** and **3′** molecules orientation, with the -Cl group in contact with either Au(111) or graphene, respectively, arises from the fact that -Cl is a sigma-donor ligand. Since both surfaces are electron-rich, the interaction is weaker, resulting in reduced binding strength. A very large BE of **2@Au(111)** is due to the formation of three strong Au−S bonds (2.650 Å; each has ≈100 kJ mol^{-1} of bond dissociation energy (BDE)).[73–75] The additional stabilization is due to other interactions such as Au●●●●H−C/O antagonistic interactions (there were 22 such interactions) with an average bond distance of 2.462 ± 0.123 Å, each reported contributing ≈17 kJ mol^{-1} leading to large BE (Figure 2a,b).[76] For the **3@graphene** surface, strong C−H●●●●π and π●●●●π

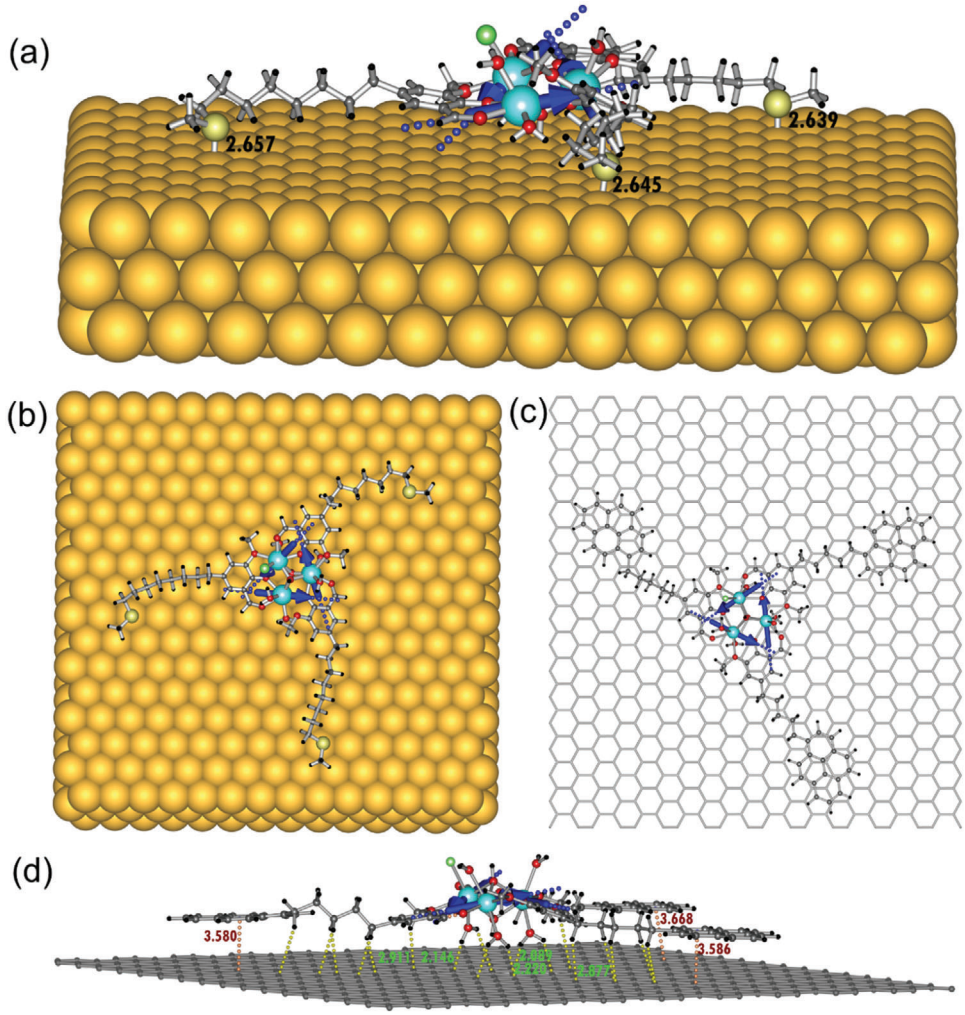

Figure 2. DFT-optimized structures of complex **2@Au(111)** and **3@graphene**. a) Side view of **2@Au(111)**, b) top view of **2@Au(111)**, c) top view of **3@graphene**, and d) side view of **3@graphene**.

interactions in the range of 3.340–3.579 Å were found, and in addition to this, we also found cation••••π interaction with Dy(III) ion, and all these weak interactions contribute to the overall BE.[77,78] A detailed analysis of the Mulliken charges reveals a net charge transfer ($\Delta\delta$) of ≈−0.18 e^- to molecule **2** and −0.26 e^- to molecule **3** from the Au(111) and graphene surface, respectively. This suggests p-type doping for both molecules; this observation is similar to earlier studies of anchoring $[Dy(CP^{ttt})_2]^+$ on SWCNT.[79]

For complexes **2** and **3** on the MgO surface, the molecule was found to decompose upon grafting, with the H atom of a H_2O molecule found to transfer to the oxygen atom of the MgO surface (Figure S3, Supporting Information). This results in the replacement of H_2O with -OH at the terminal position of Dy(III), leading to geometric distortion at the surface, indicating that the surface is likely to decompose/destroy the magnetic property of the molecule. This molecule or any molecule with terminal H_2O molecules may not survive on the MgO surface, and careful choice of the surface and molecule is required to protect the magnetic properties of the molecule.

Moreover, we optimized the pristine molecule **1** on Au(111), graphene, and MgO surfaces. The optimized structures for **1@Au(111)**, **1@graphene**, and **1@MgO** are shown in Figure S4 (Supporting Information). The results show BEs of −611 kJ mol^{-1} on Au(111) and −295 kJ mol^{-1} on graphene, while the molecule is unstable on the MgO surface due to H-atom abstraction. The BE in the case of Au(111) is still substantial due to the stronger charge transfer from the molecule to the Au(111) surface. The computed BEs suggest that the pristine molecule can be stabilized on the surface, making it suitable for device fabrication without functionalization, while the anchoring group provides higher BEs and facilitates monolayer formation. Pristine molecules with larger π-electronic clouds may have difficulty forming uniform monolayers, which is essential for controlling the toroidal moment, and stacked $\{Dy_3\}$ units may lead to toroidal moments that either cancel or enhance each other depending on their orientation and interactions.[80]

To investigate the effect of overall charge on the molecule and BE, we modeled $[Dy_3(\mu_3\text{-}OH)_2L_3Cl(H_2O)_5]Cl_3$ to $[Dy_3(\mu_3\text{-}OH)_2L_3(H_2O)_2(Cl)_4]$ on the Au(111) surface, yielding a high BE

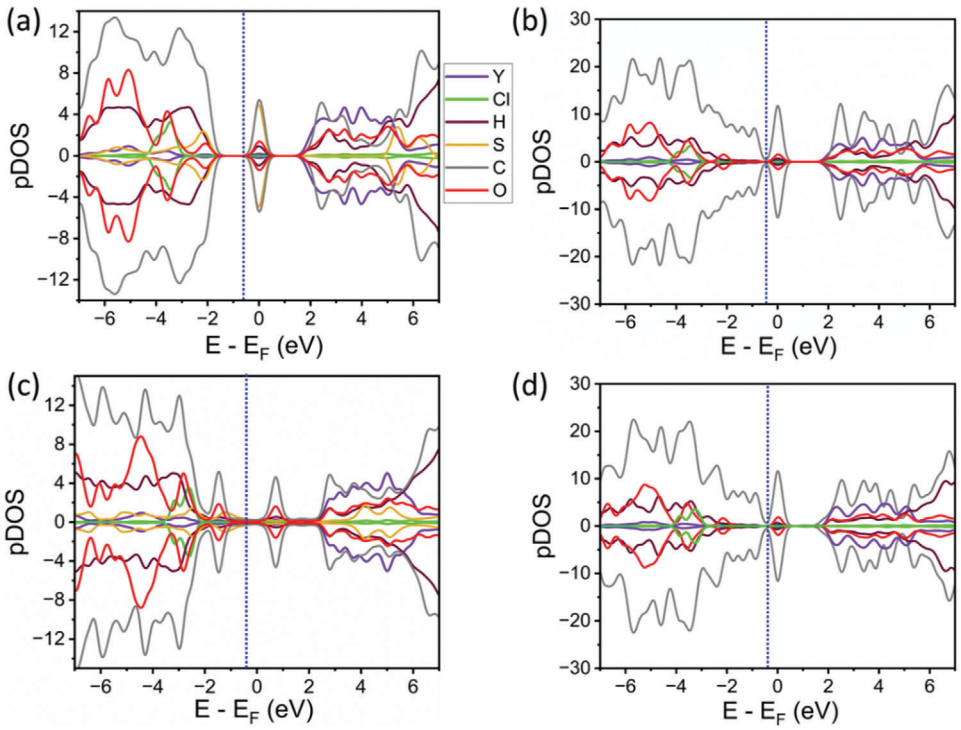

Figure 3. DFT computed pDOS of a) **2**, b) **3**, c) **2@Au(111)** and d) **3@graphene**. Here, the C atom peaks only correspond to the C-atom of the molecule only, not the graphene.

of −536.0 kJ mol^{-1}. Further, energy decomposition analysis performed for **1@Au(111)** revealed a negative deformation energy of −778 kJ mol^{-1} for the {Dy_3} molecule on Au(111) surface, indicating that the molecule adopts an energetically favorable conformation upon adsorption on the Au(111) surface compared to its pristine form. Further, analysis of the computed charge on **1@Au(111)** reveals a significant charge transfer from the hydrogen atom of the H_2O molecule to the gold atoms (≈ 0.6 e$^-$), aligning with the larger BE computed.[81]

Considering the significant stability of **1@Au(111)**, **1@graphene**, **2@Au(111)**, and **3@graphene** geometries on the surface, further calculations were performed only on these geometries. For **2@Au(111)**, the charge transfer is corroborated by changes observed in the projected density of states (pDOS). Specifically, one of the peaks associated with the sulfur atom, located near the Fermi energy, shifts from the valence band to the conduction band upon grafting. Additionally, a slight modification in the carbon atom peaks is evident, with a shift closer to the Fermi energy within the valence band. However, no significant alterations in the DOS of other atoms are observed, as these atoms do not directly interact with the surface (**Figure** 3a,c). For **3@graphene**, the strong interactions between the C-H•••π and π•••π systems are reflected in an increased DOS contribution from carbon and hydrogen atoms. This enhancement suggests significant interaction with the graphene surface. However, unlike the sulfur-based interactions on Au(111), no peak shifting between the conduction and valence bands is detected for the grafted **3@graphene** complex (Figure 3b,d). This indicates that while the π-system interactions are robust, it does not significantly alter the electronic states near the Fermi level. To further probe the electronic structure, we analyzed the orbital pDOS of the bridging {μ_3-OH} group and the metal ions. Interestingly, grafting **2** onto the Au(111) surface and **3** onto graphene causes minimal changes in their pDOS profiles. This finding suggests that the electronic environments of the {μ_3-OH} group and the metal centers remain largely intact, with the interaction between the molecules and the surfaces having a limited effect on the intrinsic electronic structure of these complexes (Figures S5 and S6, Supporting Information). Overall, while specific localized interactions between the grafted molecules and the surfaces are evident, the primary electronic characteristics of the complexes remain unaltered, underlining the stability of their electronic configurations in these hybrid systems.

3.2. Probing the Toroidal Behavior of 1, 2, and 3 at Surfaces Using Ab Initio CASSCF Calculations

As probing the toroidal properties of the **1** at the surface remains the main focus of our work, in this step, we aim to perform *ab initio* CASSCF/RASSI-SO/SINGLE_ANISO calculations to obtain the SO states corresponding to each Dy(III) centers and understand their single-ion magnetic relaxation behavior in the presence and absence of surface. As *ab initio* calculations are computationally demanding for molecules on the surfaces, we have adopted a methodology wherein the surface atoms are replaced by point charges computed from periodic DFT calculations to mimic the electrostatic effects of the surface.[82] Since

Table 1. Computed ground-state anisotropic values (g_x, g_y, g_z) for Dy1, Dy2, and Dy3 centers across all complexes.

Atom centers	Ground state anisotropy	1	1^{Opt}	2	3	1@Au(111)	1@Graphene	1@MgO	2@MgO	3@MgO	2@Au(111)	2@Graphene
Dy1	g_x	0.004	0.030	0.060	0.066	0.094	0.0309	0.000	0.024	0.006	0.173	0.035
	g_y	0.006	0.055	0.126	0.143	0.177	0.055	0.000	0.028	0.007	0.113	0.048
	g_z	19.810	19.592	19.196	19.171	19.439	19.663	19.828	19.696	19.696	19.740	19.672
Dy2	g_x	0.000	0.017	0.006	0.010	0.022	0.007	0.006	0.005	0.011	0.036	0.090
	g_y	0.001	0.025	0.010	0.019	0.035	0.013	0.007	0.005	0.016	0.061	0.154
	g_z	19.815	19.693	19.694	19.345	19.639	19.603	19.913	19.816	19.869	19.539	19.547
Dy3	g_x	0.035	0.020	0.006	0.008	0.070	0.041	0.017	0.021	0.000	0.081	0.086
	g_y	0.053	0.045	0.017	0.022	0.100	0.090	0.031	0.036	0.001	0.168	0.166
	g_z	19.769	19.570	19.725	19.705	19.371	19.234	19.506	19.572	19.865	19.445	19.410

the anisotropic properties of Dy(III) are highly sensitive to electrostatic charges but generally shielded by covalent orbital interactions due to the deeply buried 4f orbitals, this approximation is valid.[83] It has been widely adopted for studies involving surfaces and metal-organic frameworks (MOFs).[84–86] To begin with, the mechanism of relaxation at single Dy(III) centers is discussed, followed by the coupled toroidal behavior of the $\{Dy_3\}$ unit.

3.2.1. Mechanism of Magnetization Relaxation of Single-Ion Dy(III) Centers at Au(111) and Graphene Surfaces

To compute the magnetic anisotropy and spin-state energetics associated with individual Dy(III) metal centers, we performed CASSCF/RASSI-SO/SINGLE_ANISO calculations on each Dy(III) metal center, substituting other Dy(III) atoms with diamagnetic La(III) ions as both possess a similar ionic radii.[11] In the X-ray structure of **1**, the energy range of eight Kramer doublets (KDs) due to crystal field (CF) splitting (Table S2, Supporting Information) for Dy1, Dy2, and Dy3 span from 518, 581, and 444 cm^{-1}, respectively (Table S3, Supporting Information). The slight variation in the CF splitting of Dy(III) metal centers at Dy1 and Dy2 is due to the varied Dy–O bond lengths/angles and weak CF strength of the -Cl ligand atom in Dy3 (Table S1, Supporting Information). The ground state g-tensor components are: Dy1: (g_x = 0.004, g_y = 0.006, g_z = 19.810); Dy2: (g_x = 0.000, g_y = 0.001, g_z = 19.815); Dy3: (g_x = 0.035, g_y = 0.053, g_z = 19.769) (**Table 1**). The ground state wave function is highly pure, predominantly composed of the $|\pm 15/2\rangle$ state, confirming the strong Ising anisotropy in the ground state (Figure S7, Supporting Information). The LoProp charge analysis indicates that both μ_3-OH atoms have negative charges, while the other coordinated atoms counterbalance the charges on the μ_3-O, averaging out with the donor atoms (Figure S8, Supporting Information). The magnetic anisotropy direction of each Dy(III) ion aligns with the μ_3-O group of the ligand, resulting in an overall circular orientation (**Scheme 1**). A similar trend is noted for the optimized geometry of $\mathbf{1}^{opt}$ (Tables S4 and S5 and Figures S9 and S10, Supporting Information). When complex **1** is grafted onto Au(111), graphene, and MgO surfaces, the computed g_z values suggest a highly Ising nature for each Dy(III) center (Table 1). A circular orientation of the g_z anisotropy is observed in the cases of **1@Au(111)** (Tables S6 and S7 and Figures S11 and S12, Supporting Information) and **1@graphene** (Tables S8 and S9 & Figures S13 and S14, Supporting Information). In contrast, on the MgO surface, the g_z anisotropy direction is perpendicular to the Dy(III) plane, preventing the formation of a vortex arrangement of magnetic anisotropy. This change in the orientation of the g_z axis is due to higher charges (LoProp) of the OH^- ions formed from deprotonation of the H_2O molecules (Tables S10 and S11 & Figures S15 and S16, Supporting Information). The splitting of the eight lowest lying KD in **2** and **3** for Dy1 metal centers is found to be 480 cm^{-1}, a nominal drop in the CF splitting is noted compared to the X-ray geometry, and this is essentially due to relatively longer Dy-Ligand bond lengths in the optimized geometry due to removal of solid-state effects. Similar observations were also noted for the other two Dy(III) centers (Tables S12 and S13 and Figures S17 and S18 for **2**, Tables S14 and S15 and Figures S19 and S20, Supporting Information for **3**). This slight variation (up to ≈ 40 cm^{-1}) does not alter the g-anisotropy (Table S1, Supporting Information).

For complex **2@Au(111)**, the CFs of eight KDs for Dy1, Dy2, and Dy3 were found to be in 885, 663 and 462 cm^{-1}, respectively (Tables S16 and S17 and Figures S21 and S22, Supporting Information). Surprisingly, the CFs of the Dy1 enhanced significantly compared to the optimized geometry, suggesting a prominent role of Au(111) in altering the geometry (slightly shorter Dy–O/Dy–Cl bond lengths; Table S1, Supporting Information) as well as the overall crystal field strength. For Dy2 and Dy3, an enhancement in CFs is observed, although it decreases notably compared to Dy1. In Dy3, with -Cl attached, the effect is minimal, suggesting that the π-donor ability of -Cl may compensate for the larger negative charges induced by the surface.

3.2.2. Ground to the First Excited State Energy Gap

The adsorbed molecule retains Ising anisotropy even after being anchored on the surface, reflected in the computed g-values (g_x = 0.173, g_y = 0.413, g_z = 19.440 for Dy1). Similar values were also noted for the other Dy(III) centers (Table 1). In complex **3@graphene**, the energy range of eight KDs due to CF splitting

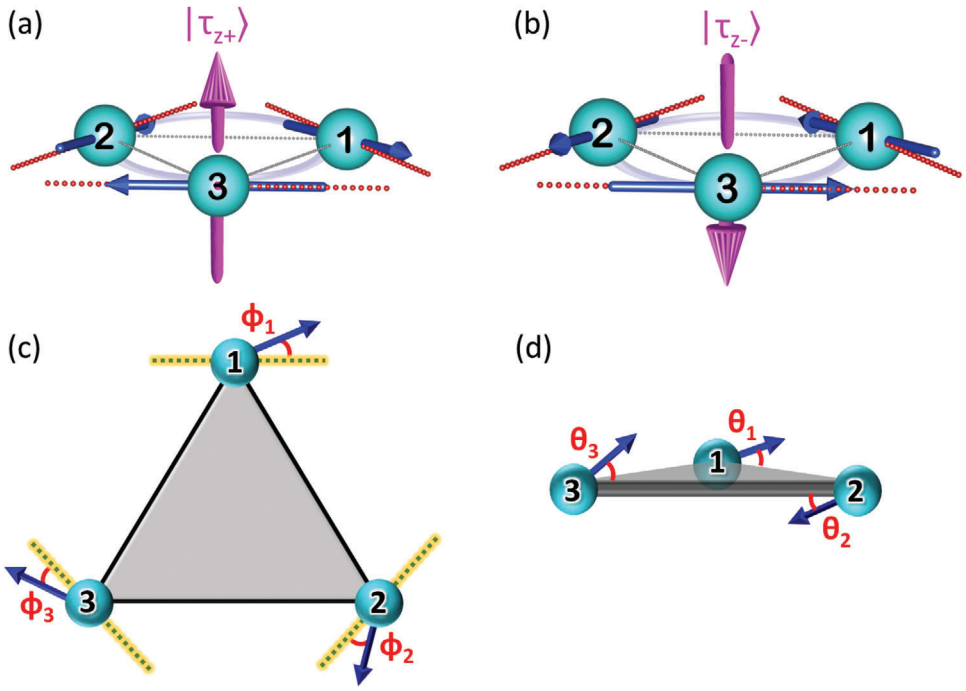

Scheme 1. The observed bistable toroidal ground state for complex **1**, with a clockwise ($|\tau_{z+}\rangle$) and anti-clockwise ($|\tau_{z-}\rangle$)orientation, displays mixed chirality and an in-plane circular moment (light blue circle). The blue arrow represents the orientation of the magnetic anisotropic axis for each Dy(III) metal center and the red dotted line represents the tangential on each Dy(III) center.

for Dy1, Dy2, and Dy3 are 551, 503, and 470 cm^{-1}, respectively. The Ising nature of anisotropy was maintained for each Dy(III) centers which are further supported by the pure $|\pm 15/2\rangle$ ground state (Tables S18 and S19 and Figures S23 and S24, Supporting Information). The tilting angle forms the tangent of each Dy(III) center (canting angle (ϕ)), and the deviation of plane angle (θ) from the anisotropic axis directions is mentioned in **Table 2**. Due to the presence of strong Ising anisotropy of each Dy(III) metal center, large CF strength, and very low quantum tunneling of magnetization (QTM)/thermally-assisted QTM (TA-QTM), each metal center shows the magnetization relaxation barrier (U_{cal}) in the range of 107–291 cm^{-1} in case of X-ray/optimized geometries of **1**. In model complexes **2** and **3**, the magnetization was found to relax via second excited KDs for Dy1 and Dy2 ion, while it is found to relax via first excited KDs in the case of Dy3. For **1@Au(111)**, magnetization relaxation occurs via the second excited state for Dy1 and Dy2, while for the Dy3 center, relaxation proceeds via the third excited state. In the case of **1@graphene**, magnetization relaxation occurs via the second excited state for Dy1, whereas for Dy2 and Dy3, relaxation occurs via the third excited state. For **1@MgO**, magnetization relaxation occurs via the second excited state for all Dy(III) centers (Dy1-Dy3), with the estimated U_{cal} lying in the range of 120–180 cm^{-1}. Similarly, for **2@Au(111)** and **3@graphene**, the Dy1-Dy3 was found to relax via the first excited state, with the estimated U_{cal} lying in the range of 78–183 cm^{-1}.

Overall, a comparison of the QTM rates, which govern the relaxation of magnetization in the Dy2 centers across all complexes,

Table 2. Computed first excited-state energy gap, deviation from the tangent (canting angle (ϕ)), and deviation from the out-of-plane angle (θ) for Dy1, Dy2, and Dy3 centers across all complexes.

Complex	ΔE [cm^{-1}]*			Canting angle [ϕ in °]			Out of plane angle [θ in °]		
	Dy1	Dy2	Dy3	Dy1	Dy2	Dy3	Dy1	Dy2	Dy3
1	191.9	178.1	153.1	7.1	7.8	4.6	2.9	8.6	0.8
1^{Opt}	90.6	114.1	107.8	7.7	7.5	6.1	4.7	6.1	1.5
2	61.4	127.6	138.9	9.8	9.0	5.5	6.7	9.4	2.1
3	57.2	75.2	131.8	8.2	9.9	3.6	4.0	3.8	5.2
1@Au(111)	98.0	147.8	98.0	8.4	11.4	12.1	8.6	9.5	10.3
1@Graphene	120.0	130.7	93.6	9.2	16.6	13.3	7.6	7.5	11.0
2@Au(111)	78.0	132.7	99.2	12.3	11.1	8.3	7.1	5.7	9.9
3@Graphene	118.2	109.3	102.8	11.6	8.1	9.6	12.0	4.9	11.3

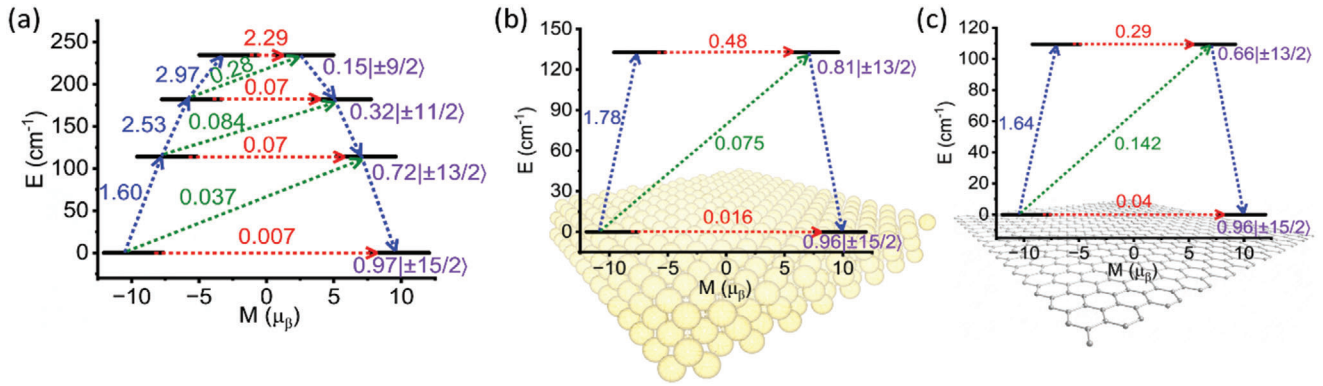

Figure 4. Single-ion magnetization relaxation dynamics of the Dy2 centers: a) **1^{opt}**, b) **2@Au(111)**, and c) **3@graphene**.

reveals notable variations. Among all the centers, Dy2 exhibits the best performance, with QTM rates measured as follows: 0.0002 μ_B for complex **1**, 0.007 for the **1^{opt}**, 0.009 for **1@Au(111)**, 0.003 for **1@graphene**, 0.002 for **1@MgO**, 0.005 for complex **2**, 0.002 for **3**, 0.016 for **2@Au(111)**, and 0.04 for **3@graphene**. These differences highlight how structural modifications influence magnetic relaxation dynamics. Wavefunction analysis further supports these observations, indicating that the ground state remains highly Ising in nature, predominantly originating from the $|\pm15/2\rangle$ state in all cases. However, anchoring on different surfaces induces a change in the first excited KD states with 91% pure $|\pm13/2\rangle$ state for complex **1** with the increase in the percent of mixing with other m_J states in the following order **1 < 1@MgO < 1@Au(111) ≈ 1@graphene < 2@Au(111) < 1^{opt} < 2 < 3 < 3@graphene** (**Figure 4**). These findings suggest that structural and electronic variations within the complexes influence the QTM rates and the excited state mixing, altering their single-ion magnetic anisotropy.

3.2.3. Analysis of Exchange-Coupled States and Toroidal Moments on Au(111) and Graphene Surfaces

After establishing the single-ion behavior of molecules on the surface, we move to understand the magnetic/toroidal behavior of $\{Dy_3\}$ cluster on the surface. For this, the magnetic coupling between the Dy(III) ions needs to be estimated. To calculate the magnetic exchange interaction between Dy(III) metal centers, we employed the broken-symmetry DFT (BS-DFT) method, where Dy(III) ions were substituted with an isotropic Gd(III) ion (computational details). The isotropic magnetic exchange (J) for complex **1** was determined to be −0.093 cm^{-1}, while the **1^{opt}** yielded J = -0.125 cm^{-1}. The average Dy–O–Dy bond angle was ≈97.4° for both geometries, aligning with earlier magneto-structural correlations that predict antiferromagnetic coupling for angles in this range.[83] These values confirm weak antiferromagnetic exchange interactions, with minor variations attributed to slight geometric changes (Table S1, Supporting Information). Similar values for the X-ray and DFT optimized geometry suggest that slight structural variation does not influence the sign/strength of J_s significantly. Additionally, the computed spin density plots for **1** and **1^{opt}** reveal a significant negative spin density (−0.1) on the μ_3-OH bridge, indicative of a spin polarization mechanism (Figure S25, Supporting Information). Similarly, the spin density plots for **2@Au(111)** and **3@graphene** show negative spin densities localized on the μ_3-OH bridge, the sulfur atom of the alkyl chain, and the pyrene ring, respectively (Figure S5, Supporting Information). This suggests active spin interactions between the molecule and the surface, supporting the surface-mediated stabilization of magnetic properties hypothesis (**Figure 5**).

To estimate the magnetic coupling corresponding to the Dy(III) ion and also to obtain the dipolar contributions to the J values, we have employed the Lines model[87] considering the following Ising Hamiltonian (equation S2, Supporting Information) where the sign of the dipolar coupling depends on the angle between the orientation of the magnetic moments and the vector connecting two interacting centers, which denoted as ϕ. It has been observed that if the angle ϕ > 54.75°, then the interaction is expected to be antiferromagnetic, while ϕ < 54.75° is expected to yield ferromagnetic coupling. Further, the magnitude of J depends on the magnetic moment and distance between the coupling sites (the computational section in the ESI).

First, we simulated the powder magnetic susceptibility and magnetization for complex **1** and computed the best fitting parameter of J = −0.57 cm^{-1} (Figures S26 and Table S20, Supporting Information). The computed J value is similar to that estimated for the $\{Dy_3\}$ complexes earlier.[13] Since the first excited states of all three single-ion Dy(III) centers in **1** are much higher in energy (>153 cm^{-1}) than computed exchange couplings, it is safe to only account for the excited states in plotting the Zeeman diagram. As a result, the Zeeman spectrum (Figure S26, Supporting Information) displays the evolution of the lowest exchange-coupled states in an applied magnetic field. As one can see, the ground state can be described $|\tau_{z\pm}\rangle = |\pm1, \pm1, \pm1\rangle$ as with magnetic moment directions of three Dy(III) sites, forming a clockwise $|\tau_{z+}\rangle$ or counterclockwise $|\tau_{z-}\rangle$ toroidal moment. The second counterclockwise component is obtained by a time-inversion operation that changes the directions of all the magnetic moments; due to this, we observed a bistable nonmagnetic toroidal ground state. The experimentally reported micro-squid data of **1** suggests the magnetization is almost zero even at very low temperatures up to ≈0.8 T, which suggests the toroidal blocking of complex **1** is up to ≈0.8 T. To validate our methodology, we checked the toroidal blocking using Zeeman spectra

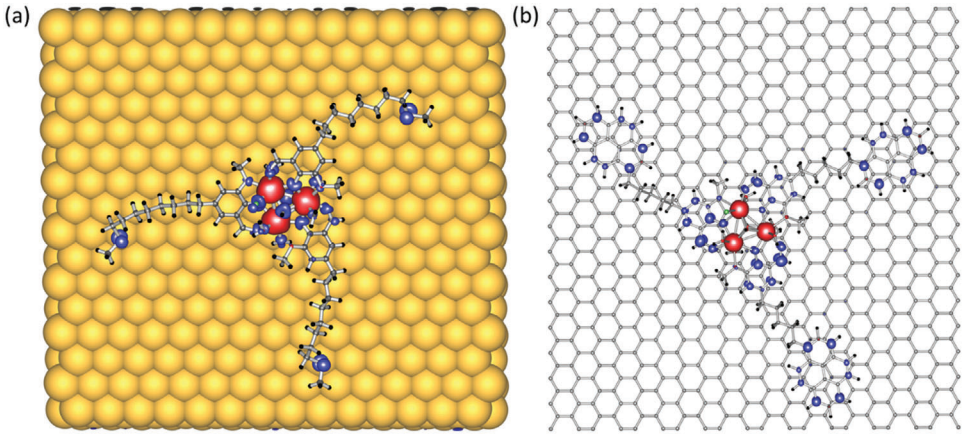

Figure 5. DFT computed spin density plots of the adsorbed molecule on the surface are shown for a) **2@Au(111)** and b) **3@graphene**, highlighting the distribution of spin density across the molecular framework and its interaction with the surface (drawn for a value of 0.009 e^- $bohr^{-3}$). Here, red represents positive spin density, while blue represents negative spin density.

and found no level-crossing up to ≈ 0.8 T; this further suggests that the computed exchange and *ab initio* energies very well explain the previously reported toroidal behavior of complex **1**.[13] Similarly, we have simulated the magnetic susceptibility and magnetization for $\mathbf{1}^{opt}$ with various exchange coupling. We found that the $J = -0.61$ cm^{-1} reproduces the magnetic and Zeeman spectra well (Figures S27 and Table S21, Supporting Information). The computed magnetic exchange coupling for complexes **2** and **3** (**Table 3**), the simulated magnetic and Zeeman spectrum, and the low-lying exchange coupled states are in Tables S22 and S23 and Figure S28 (Supporting Information) for **3**, respectively. Both **2** and **3** very well predict the toroidal behavior and show toroidal blocking similar to **1**.

To compute the exchange coupled state on surfaces, first, we compute the dipolar coupling (using equation S2, Supporting Information), which helps to stabilize the low-lying toroidal states. Here, we also found a similar trend of magnetic exchange coupling, which is antiferromagnetic: $J = -0.60$ cm^{-1} for **1@Au(111)** and **1@graphene**, $J = -0.61$ cm^{-1} for **2@Au(111)** and $J = -0.62$ cm^{-1} for **3@graphene**. The magnetic exchange couplings are comparable, but slight variations in dipolar coupling arise due to differences in the magnetic moments and radii (*r*). In **1@Au(111)** and **1@graphene**, the low-lying exchange-coupled states are located at 6.9 and 6.6 cm^{-1}, respectively (Tables S24 and S25, Supporting Information). The Zeeman splitting diagrams reveal a level crossing at 0.75 T for **1@Au(111)** and 0.76 T for **1@graphene** (Figures S29 and S30, Supporting Information, respectively). For **2@Au(111)**, the first excited low-lying energy state lies at 9.8 cm^{-1}, and **Figure 6b** illustrates the evolution of the lowest exchange-coupled states under an applied magnetic field (Table S26, Supporting Information). The ground state is nonmagnetic, with a level crossing at ≈ 1.2 T (Figure 6c). For **3@graphene**, the first excited is slightly lower in energy at 6.8 cm^{-1}, thanks to slightly weaker *J* values (Table S27, Supporting Information). This is also reflected in the Zeeman level diagram, which predicts a crossover at the lower field of ≈ 0.83 T (Figure 6f) compared to **2@Au(111)**.

For complexes **1@Au(111)**, **1@graphene**, **2@Au(111)**, and **3@graphene**, the total magnetic moment in the ground exchange pseudo-doublet state ($\mu_z = 1/2\ g_z\mu_B$) is calculated as 0.92, 0.89, 2.04 and 1.27 μ_B, respectively. These values align with the nonzero magnetization observed at low temperatures, consistent with earlier studies on $\{Dy_3\}$ triangles and their characteristic magnetic behavior. These findings highlight the significant interaction of the molecule with the surface, particularly on the Au(111) surface. The chemical adsorption of **2@Au(111)** results in an increased gap of the ground-first-excited exchange-coupled state, effectively stabilizing the molecule and enhancing the toroidal blockade greater than 1 T. As the Au(111) surface demonstrates slightly better performance than graphene, it underscores the potential of such molecules for applications in quantum sensors and nanoscale magnetometers, where robustness against external perturbations is essential. Furthermore, this enhanced stability positions **2@Au(111)** as a promising candidate for spintronic devices, where its superior spin-filtering properties enable more reliable and efficient control of spin dynamics, paving the way for advanced technological applications such as quantum information processing and high-precision magnetic sensing systems.

Table 3. The computed magnetic exchange interactions for all the complexes (in cm^{-1}).

	1	1^{opt}	2	3	1@Au(111)	1@Graphene	2@Au(111)	3@Graphene
$J_{exc.}$	−0.093	−0.125	−0.125	−0.125	−0.125	−0.125	−0.125	−0.125
$J_{dip.}$	−0.477	−0.485	−0.465	−0.475	0.475	−0.475	−0.485	−0.495
J_{total}	−0.57	−0.61	−0.59	−0.60	−0.60	−0.60	−0.61	−0.62

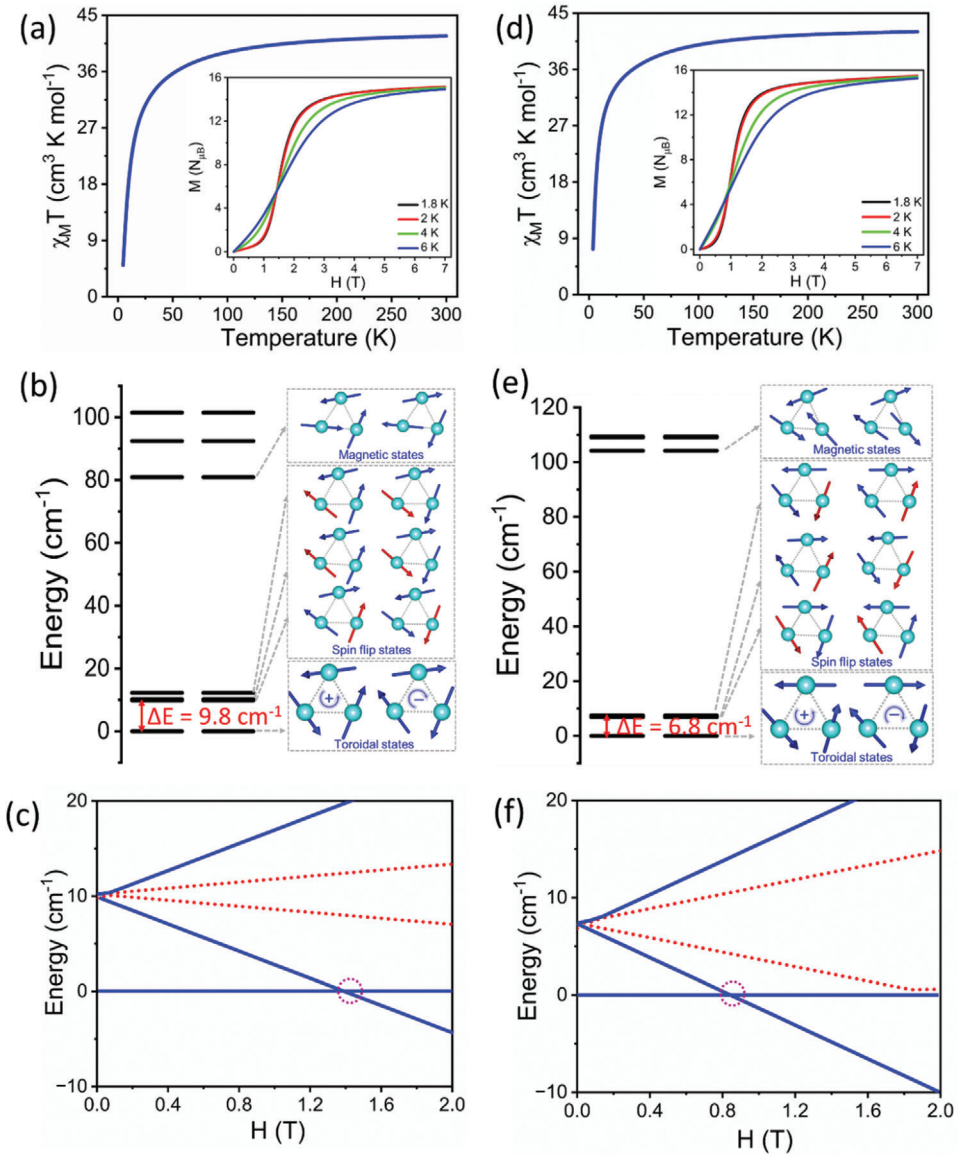

Figure 6. Simulated magnetic susceptibility, variable-temperature isothermal magnetization (inset), low-lying energy states, and Zeeman spectrum using the POLY_ANISO Lines model a–c) for **2@Au(111)** and d–f) for **3@graphene**. The pink circles in Figures (c) and (d) highlight toroidal blocking.

4. Conclusion

Stabilizing the toroidal ground state at the molecular level presents significant challenges due to the sensitivity of these states to the ligand framework and thermal fluctuations. Grafting such molecules onto surfaces for practical applications is even more demanding, as it requires stabilization of the molecule on the surface and the retention of its single-molecule toroidal (SMT) behavior post-grafting. In this study, we have selected a $\{Dy_3\}$ triangular complex and investigated its interaction with a range of surfaces, including metallic (Au(111)), conductive (graphene), and non-metallic (MgO) substrates, through in silico periodic density functional theory in combination with *ab initio* CASSCF/RASSI_SO/SINGLE_ANISO/POLY_ANISO calculations. Our results reveal that the single-ion behavior of the $\{Dy_3\}$ centers can be modified depending on the surface, likely due to differences in relaxation rates and the gap between energy levels. For pristine **1@Au(111)** and **1@graphene**, the low-lying exchange-coupled states are located at 6.9 and 6.6 cm^{-1}, respectively, with level crossings predicted at 0.75 and 0.76 T. Functionalization with pyrene (**2**), and $(CH_2)_8$-S (**3**) linkers further modify the toroidal behavior. Notably, **2@Au(111)** exhibits an increased energy gap of 9.8 cm^{-1}, leading to a significantly higher toroidal blocking field of 1.2 T compared to 0.75 T for pristine **1@Au(111)**. Similarly, **3@graphene** achieves a blocking field of 0.83 T, which is enhanced compared to 0.76 T for pristine **1@graphene**. These enhancements can be attributed to stronger surface interactions facilitated by functionalization, which stabilizes the molecule on the surface. The computed BEs support strong anchoring of molecules on both Au(111) and graphene

surfaces. However, our calculations indicate that molecules undergo decomposition on the MgO surface, disrupting toroidal behavior. The analysis of low-lying exchange-coupled states across all systems suggests that the toroidal moment of these $\{Dy_3\}$ complexes is preserved post-grafting.

These findings suggest that chemical adsorption and surface interactions are critical in stabilizing the toroidal ground state and enhancing the toroidal blocking, particularly for Au(111)-grafted complexes. For the first time, we reveal that toroidal behavior can be preserved on surfaces and substantially amplified depending on surface characteristics and functionalization. This opens promising avenues for leveraging electrically controllable quantum states in advanced technologies such as quantum sensors, nanoscale magnetometers, and spintronics.

Supporting Information

Supporting Information is available from the Wiley Online Library or from the author.

Acknowledgements

The authors thank DST and SERB (CRG/2018/00430; DST/CSA-03/2018-10; SB/SJF/2019-20/12) for funding. DC thanks UGC, and RKT thanks CSIR for the SRF fellowship.

Conflict of Interest

The author declares no conflicts of interest.

Data Availability Statement

The data that support the findings of this study are available in the supplementary material of this article.

Keywords

Au(111) surface, DFT and ab initio CASSCF calculations, Dy3 SMMs, single molecule toroics

Received: December 17, 2024
Revised: February 3, 2025
Published online: February 21, 2025

[1] D. A. McQuarrie, J. D. Simon, *Physical Chemistry*, University Science Books, Sausalito, CA **1997**.
[2] D. J. Griffiths, *Introduction to Electrodynamics*, Cambridge University Press, Cambridge, UK **2023**.
[3] B. B. Van Aken, J.-P. Rivera, H. Schmid, M. Fiebig, *Nature* **2007**, *449*, 702.
[4] K. M. Rabe, *Nature* **2007**, *449*, 674.
[5] I. B. Zel'Dovich, *Sov. Phys. JETP* **1958**, *6*, 1184.
[6] A. Ceulemans, L. Chibotaru, P. Fowler, *Phys. Rev. Lett.* **1998**, *80*, 1861.
[7] N. A. Spaldin, M. Fiebig, M. Mostovoy, *J. Condens. Matter Phys.* **2008**, *20*, 434203.
[8] C. Ederer, N. A. Spaldin, *Phys. Rev. B Condens. Matter* **2007**, *76*, 214404.
[9] H. Wang, Z. Zhu, L. Droitte, W. Liao, O. Cador, B. Le Guennic, J. Tang, *Chem. Sci.* **2023**, *14*, 7208.
[10] J. Tang, I. Hewitt, N. Madhu, G. Chastanet, W. Wernsdorfer, C. E. Anson, C. Benelli, R. Sessoli, A. K. Powell, *Angew Chem. Int. Ed.* **2006**, *45*, 1729.
[11] L. Ungur, W. Van den Heuvel, L. F. Chibotaru, *New J. Chem.* **2009**, *33*, 1224.
[12] M. Gysler, F. El Hallak, L. Ungur, R. Marx, M. Hakl, P. Neugebauer, Y. Rechkemmer, Y. Lan, I. Sheikin, M. Orlita, *Chem. Sci.* **2016**, *7*, 4347.
[13] L. Chibotaru, L. Ungur, A. Soncini, *Angew Chem. Int. Ed.* **2008**, *47*, 4126.
[14] J. Luzon, K. Bernot, I. J. Hewitt, C. E. Anson, A. K. Powell, R. Sessoli, *Phys. Rev. Lett.* **2008**, *100*, 247205.
[15] L. Ungur, S.-Y. Lin, J. Tang, L. F. Chibotaru, *Chem. Soc. Rev.* **2014**, *43*, 6894.
[16] K. R. Vignesh, G. Rajaraman, *ACS Omega* **2021**, *6*, 32349.
[17] A. Zabala-Lekuona, J. M. Seco, E. Colacio, *Coord. Chem. Rev.* **2021**, *441*, 213984.
[18] L. Tacconi, S. S. Leiszner, M. Briganti, G. Cucinotta, E. Otero, M. Mannini, M. Perfetti, *Small* **2024**, *20*, 2401627.
[19] M. Briganti, E. Lucaccini, L. Chelazzi, S. Ciattini, L. Sorace, R. Sessoli, F. Totti, M. Perfetti, *J. Am. Chem. Soc.* **2021**, *143*, 8108.
[20] A. S. Manvell, R. Pfleger, N. A. Bonde, M. Briganti, C. A. Mattei, T. B. Nannestad, H. Weihe, A. K. Powell, J. Ollivier, J. Bendix, *Chem. Sci.* **2024**, *15*, 113.
[21] D. Chauhan, K. R. Vignesh, A. Swain, S. K. Langley, K. S. Murray, M. Shanmugam, G. Rajaraman, *Cryst. Growth Des.* **2022**, *23*, 197.
[22] X.-L. Li, J. Tang, *Dalton Trans.* **2019**, *48*, 15358.
[23] X. L. Li, Z. Ma, J. Tang, *Chem.-Eur. J.* **2024**, *30*, 202304369.
[24] S. K. Langley, K. R. Vignesh, T. Gupta, C. J. Gartshore, G. Rajaraman, C. M. Forsyth, K. S. Murray, *Dalton Trans.* **2019**, *48*, 15657.
[25] K. Hymas, A. Soncini, K. R. Vignesh, D. Chauhan, A. Swain, S. L. Benjamin, D. Borah, M. Shanmugam, W. Wernsdorfer, G. Rajaraman, *npj Quantum Mater.* **2024**, *9*, 106.
[26] P.-H. Guo, J.-L. Liu, Z.-M. Zhang, L. Ungur, L. F. Chibotaru, J.-D. Leng, F.-S. Guo, M.-L. Tong, *Inorg. Chem.* **2012**, *51*, 1233.
[27] S. Mondal, D. Chauhan, T. Guizouarn, F. Pointillart, G. Rajaraman, A. Steiner, V. Baskar, *Inorg. Chem.* **2024**, *63*, 22338.
[28] L. Ungur, S. K. Langley, T. N. Hooper, B. Moubaraki, E. K. Brechin, K. S. Murray, L. F. Chibotaru, *J. Am. Chem. Soc.* **2012**, *134*, 18554.
[29] J. Lu, V. Montigaud, O. Cador, J. Wu, L. Zhao, X.-L. Li, M. Guo, B. Le Guennic, J. Tang, *Inorg. Chem.* **2019**, *58*, 11903.
[30] S. K. Langley, K. R. Vignesh, B. Moubaraki, G. Rajaraman, K. S. Murray, *Chem.-Eur. J.* **2019**, *25*, 4156.
[31] Q. Zhang, M. L. Baker, S. Li, M. P. Sarachik, J. J. Baldoví, A. Gaita-Ariño, E. Coronado, D. I. Alexandropoulos, T. C. Stamatatos, *Nanoscale* **2019**, *11*, 15131.
[32] S. Y. Lin, W. Wernsdorfer, L. Ungur, A. K. Powell, Y. N. Guo, J. Tang, L. Zhao, L. F. Chibotaru, H. J. Zhang, *Angew. Chem., Int. Ed.* **2012**, *51*, 12767.
[33] X.-L. Li, J. Wu, J. Tang, B. Le Guennic, W. Shi, P. Cheng, *Chem. Commun.* **2016**, *52*, 9570.
[34] G. Novitchi, G. Pilet, L. Ungur, V. V. Moshchalkov, W. Wernsdorfer, L. F. Chibotaru, D. Luneau, A. K. Powell, *Chem. Sci.* **2012**, *3*, 1169.
[35] H. Kaemmerer, A. Baniodeh, Y. Peng, E. Moreno-Pineda, M. Schulze, C. E. Anson, W. Wernsdorfer, J. Schnack, A. K. Powell, *J. Am. Chem. Soc.* **2020**, *142*, 14838.
[36] H.-L. Zhang, Y.-Q. Zhai, L. Qin, L. Ungur, H. Nojiri, Y.-Z. Zheng, *Matter* **2020**, *2*, 1481.
[37] J. Wu, X.-L. Li, M. Guo, L. Zhao, Y.-Q. Zhang, J. Tang, *Chem. Commun.* **2018**, *54*, 1065.
[38] K. R. Vignesh, A. Soncini, S. K. Langley, W. Wernsdorfer, K. S. Murray, G. Rajaraman, *Nat. Commun.* **2017**, *8*, 1023.

[39] K. R. Vignesh, S. K. Langley, A. Swain, B. Moubaraki, M. Damjanović, W. Wernsdorfer, G. Rajaraman, K. S. Murray, *Angew. Chem., Int. Ed.* **2018**, *57*, 779.
[40] G. Fernandez Garcia, D. Guettas, V. Montigaud, P. Larini, R. Sessoli, F. Totti, O. Cador, G. Pilet, B. Le Guennic, *Angew. Chem., Int. Ed.* **2018**, *57*, 17089.
[41] A. Popov, D. Plokhov, A. Zvezdin, *Phys. Rev. B* **2016**, *94*, 184408.
[42] J. M. Crabtree, A. Soncini, *Phys. Rev. B* **2018**, *98*, 094417.
[43] D. Plokhov, A. Pyatakov, A. Popov, A. K. Zvezdin, In *Single Molecule Toroics: Synthetic Strategies, Theory and Applications*, Springer, New York **2022**.
[44] S. Sanvito, *Chem. Soc. Rev.* **2011**, *40*, 3336.
[45] A. R. Rocha, V. M. Garcia-Suarez, S. W. Bailey, C. J. Lambert, J. Ferrer, S. Sanvito, *Nat. Mater.* **2005**, *4*, 335.
[46] R. K. Tiwari, R. Nabi, R. L. Kumawat, B. Pathak, G. Rajaraman, *Inorg. Chem.* **2023**, *63*, 316.
[47] M. Mannini, F. Bertani, C. Tudisco, L. Malavolti, L. Poggini, K. Misztal, D. Menozzi, A. Motta, E. Otero, P. Ohresser, *Nat. Commun.* **2014**, *5*, 4582.
[48] G. Gabarró-Riera, G. Aromí, E. C. Sañudo, *Coord. Chem. Rev.* **2023**, *475*, 214858.
[49] R. K. Tiwari, R. Paul, G. Rajaraman, *Dalton Trans.* **2024**, *53*, 14623.
[50] M. Mannini, F. Pineider, P. Sainctavit, C. Danieli, E. Otero, C. Sciancalepore, A. M. Talarico, M.-A. Arrio, A. Cornia, D. Gatteschi, *Nat. Mater.* **2009**, *8*, 194.
[51] G. Serrano, L. Poggini, M. Briganti, A. L. Sorrentino, G. Cucinotta, L. Malavolti, B. Cortigiani, E. Otero, P. Sainctavit, S. Loth, *Nat. Mater.* **2020**, *19*, 546.
[52] A. Candini, S. Klyatskaya, M. Ruben, W. Wernsdorfer, M. Affronte, *Nano Lett.* **2011**, *11*, 2634.
[53] C. Wäckerlin, F. Donati, A. Singha, R. Baltic, S. Rusponi, K. Diller, F. Patthey, M. Pivetta, Y. Lan, S. Klyatskaya, *Adv. Mater.* **2016**, *28*, 5195.
[54] L. Spree, F. Liu, V. Neu, M. Rosenkranz, G. Velkos, Y. Wang, S. Schiemenz, J. Dreiser, P. Gargiani, M. Valvidares, *Adv. Funct. Mater.* **2021**, *31*, 2105516.
[55] M. Briganti, F. Totti, In *Computational Modelling of Molecular Nanomagnets*, Springer, New York **2023**.
[56] B. G. Lippert, J. H. Parrinello, Michele, *Mol. Phys.* **1997**, *92*, 477.
[57] D. Aravena, E. Ruiz, *J. Am. Chem. Soc.* **2012**, *134*, 777.
[58] A. Lunghi, M. Iannuzzi, R. Sessoli, F. Totti, *J. Mater. Chem. C.* **2015**, *3*, 7294.
[59] J.-C. Ren, J. Zhou, S. Li, W. Liu, *J. Phys. Chem. C* **2023**, *127*, 15699.
[60] F. Donati, M. Pivetta, C. Wolf, A. Singha, C. Wäckerlin, R. Baltic, E. Fernandes, J.-G. De Groot, S. L. Ahmed, L. Persichetti, *Nano Lett.* **2021**, *21*, 8266.
[61] E. Ruiz, J. Cano, S. Alvarez, P. Alemany, *J. Comput. Chem.* **1999**, *20*, 1391.
[62] T. R. Cundari, W. J. Stevens, *J. Chem. Phys.* **1993**, *98*, 5555.
[63] M. J. Frisch, G. W. Trucks, H. B. Schlegel, G. E. Scuseria, M. A. Robb, J. R. Cheeseman, G. Scalmani, V. Barone, G. A. Petersson, H. Nakatsuji, X. Li, M. Caricato, A. V. Marenich, J. Bloino, B. G. Janesko, R. Gomperts, B. Mennucci, H. P. Hratchian, J. V. Ortiz, A. F. Izmaylov, J. L. Sonnenberg, F. Ding, F. Lipparini, F. Egidi, J. Goings, B. Peng, A. Petrone, T. Henderson, D. Ranasinghe, V. G. Zakrzewski, et al., *Gaussian 16 Rev. C.01*, Gaussian,Inc., Wallingford, CT **2016**.
[64] M. K. Singh, N. Yadav, G. Rajaraman, *Chem. Commun.* **2015**, *51*, 17732.
[65] F. Aquilante, J. Autschbach, R. K. Carlson, L. F. Chibotaru, M. G. Delcey, L. De Vico, F. Galván, N. Ferré, L. M. Frutos, L. Gagliardi, *J. Comput. Chem.* **2016**, *37*, 506.
[66] P. Å. Malmqvist, B. O. Roos, B. Schimmelpfennig, *Chem. Phys. Lett.* **2002**, *357*, 230.
[67] B. O. Roos, P.-Å. Malmqvist, *Phys. Chem. Chem. Phys.* **2004**, *6*, 2919.
[68] B. A. Heß, C. M. Marian, U. Wahlgren, O. Gropen, *Chem. Phys. Lett.* **1996**, *251*, 365.
[69] B. O. Roos, R. Lindh, P.-Å. Malmqvist, V. Veryazov, P.-O. Widmark, A. C. Borin, *J. Phys. Chem. A* **2008**, *112*, 11431.
[70] L. F. Chibotaru, L. Ungur, *J. Chem. Phys.* **2012**, *137*, 064112.
[71] L. Chibotaru, L. Ungur, The computer programs SINGLE_-ANISO and POLY_ANISO; University of Leuven, 2006.
[72] S. M. Avdoshenko, *J. Comput. Chem.* **2018**, *39*, 1594.
[73] S. Feng, N. Luo, A. Tang, W. Chen, Y. Zhang, S. Huang, W. Dou, *J. Phys. Chem. C* **2019**, *123*, 16614.
[74] D. L. Kokkin, R. Zhang, T. C. Steimle, I. A. Wyse, B. W. Pearlman, T. D. Varberg, *J. Phys. Chem. A* **2015**, *119*, 11659.
[75] G. Rajaraman, A. Caneschi, D. Gatteschi, F. Totti, *Phys. Chem. Chem. Phys.* **2011**, *13*, 3886.
[76] H. Schmidbaur, H. G. Raubenheimer, L. Dobrzańska, *Chem. Soc. Rev.* **2014**, *43*, 345.
[77] M. Nishio, M. Hirota, Y. Umezawa, *The CH/π interaction: Evidence, nature, and consequences*, John Wiley & Sons, Hoboken, New Jersey **1998**.
[78] D. A. Dougherty, *Science* **1996**, *271*, 163.
[79] R. Nabi, R. K. Tiwari, G. Rajaraman, *Chem. Commun.* **2021**, *57*, 11350.
[80] J. Dreiser, A. M. Ako, C. Wäckerlin, J. Heidler, C. E. Anson, A. K. Powell, C. Piamonteze, F. Nolting, S. Rusponi, H. Brune, *J. Phys. Chem. C* **2015**, *119*, 3550.
[81] Y. Santiago-Rodriguez, J. A. Herron, M. C. Curet-Arana, M. Mavrikakis, *Surf. Sci.* **2014**, *627*, 57.
[82] A. Sarkar, G. Rajaraman, *Chem. Sci.* **2020**, *11*, 10324.
[83] T. Rajeshkumar, S. K. Singh, G. Rajaraman, *Polyhedron* **2013**, *52*, 1299.
[84] R. Nabi, G. Rajaraman, *Chem. Commun.* **2019**, *55*, 8238.
[85] R. Jose, S. Pal, G. Rajaraman, *Chem. Commun.* **2023**, *59*, 10315.
[86] R. Jose, S. Kancharlapalli, T. K. Ghanty, S. Pal, G. Rajaraman, *Chem.-Eur. J.* **2022**, *28*, 202104526.
[87] M. Lines, *J. Chem. Phys.* **1971**, *55*, 2977.